


Rashba spin-orbit coupling induced modulation of magnetic anisotropy in canted antiferromagnetic heterostructures

Megha Vagadia,^{*} Jayaprakash Sahoo, Ankit Kumar[✉], Suman Sardar, Tejas M. Tank[✉], and D. S. Rana^{✉†}
Department of Physics, Indian Institute of Science Education and Research Bhopal, Bhopal, Madhya Pradesh 462066, India

 (Received 28 July 2022; accepted 30 January 2023; published 17 February 2023)

The combined effect of charge transfer, broken symmetries, and spin-orbit coupling (SOC) yields interfacial magnetism and transport in spatially asymmetric quantum oxide heterostructures. The polar nature of such interfaces activates the Rashba effect which provides a platform to modify the electronic band structure, whereas the presence of competing magnetic anisotropies is essential for deriving the topologically nontrivial spin textures. Entanglement of these two effects wherein the Rashba physics can be utilized to manipulate magnetic anisotropy (MA) is contemplated as a pathway to alternative electronic states. Here, using the $\text{CaMnO}_3/\text{CaIrO}_3$ heterostructure as a template, we demonstrate that Rashba SOC modulates the MA and controls the sign and magnitude of anomalous Hall conductivity consequent to the modification in the electronic band structure via the reconstruction of Berry curvature. This approach to tune and control the multipronged magnetotransport phenomena via Rashba SOC (without external bias voltage) is potentially relevant for spin-orbitronics functionalities.

DOI: [10.1103/PhysRevB.107.064420](https://doi.org/10.1103/PhysRevB.107.064420)

In complex quantum materials, spontaneous symmetry breaking is at the core of emergent phases such as superconductivity, antiferromagnetism (AFM), and ferroelectricity [1,2]. In recent times, breaking of the space inversion symmetry in the spin-orbit coupled (SOC) systems has been explored for the efficient spin-to-charge interconversion—a feature that is driving the development of the emerging field of spin-orbitronics [3–5]. Here, spatial asymmetry at the two-dimensional (2D) interfaces induces the perpendicular built-in electric field which, in the presence of SOC, lifts the degeneracy of the electronic band structure with the momentum-dependent spin-split subbands. Charge carriers passing through this electric field experience an effective magnetic field that gives rise to momentum-dependent Zeeman energy—also known as the Rashba SOC [6,7]. The associated Rashba Hamiltonian is written as $H_R = \alpha_R(k \times \sigma) \cdot z$, where σ is the vector of the Pauli spin matrices, z is the unit vector perpendicular to the interface, k is the momentum, and α_R is the Rashba coefficient which varies linearly with the electric field and SOC.

In SOC systems, the presence of an electric field perturbs the trajectory of the electron based on the direction of the angular momentum. This anomalous contribution to the velocity is induced by the Lorentz force produced by the Berry curvature $\Omega(p) \propto \alpha_R \nabla_p \times (\sigma \times p)$, which depends on the intrinsic properties of occupied electronic states [8]. Nonvanishing Berry curvature in systems with broken time-reversal symmetry gives rise to off-diagonal conductivity which contributes to the intrinsic anomalous Hall effect (AHE). Various intriguing physical properties of Rashba materials are

explained in the context of Berry curvature and the associated Berry phase. The resultant modification in the velocity due to the Rashba effect can be deduced according to $V_a = \partial_p \hat{H}_R = -(\alpha_R/\hbar)z \times \sigma$ [3].

In $3d-5d$ transition-metal-based heterostructures, SOC has been key in realizing varieties of exotic phenomena at the interface such as spin-momentum locking, magnetic phases, intrinsic AHE, and topologically nontrivial spin textures [9–12]. In addition, charge transfer in oxide heterostructures build voltage potential across the interface that activates the Rashba effect [13]. The entanglement of the spin and orbital degrees of freedom in these heterostructures can be executed through the Rashba effect in controlling and manipulating the spin currents. Further, SOC along with crystal symmetry determines the magnetic anisotropy (MA) of the materials. Hence, interfacial spin-based phenomena and magnetic textures can be controlled and tuned intrinsically by SOC. The competing MAs can lead to noncollinear spin texture with topological band structure. Extrinsic modulation of MA can be driven by the applied electric field or exchange bias (EB). However, studies elucidating SOC-controlled MA are much needed but are rare. Also, the change in the easy axis is reported for the different heterostructures which presents hindrance in realizing switching-based memory devices.

Despite promising transport phenomena induced by Rashba SOC in the presence of effective bias voltage at the oxide interfaces [13–15], the challenge is to enhance and control Rashba SOC in the absence of bias voltage for the energy-efficient spin-orbitronics application. In this paper, we present transport studies on $\text{CaMnO}_3/\text{CaIrO}_3$ heterostructures, having charge transfer from the Ir to the Mn site at the interface that varies with the constituent layer thickness. In its ground state, CaIrO_3 is a paramagnetic semimetal. In low dimensions, the CaIrO_3 period possesses a larger

^{*}mvagadia@iiserb.ac.in

[†]dsrana@iiserb.ac.in

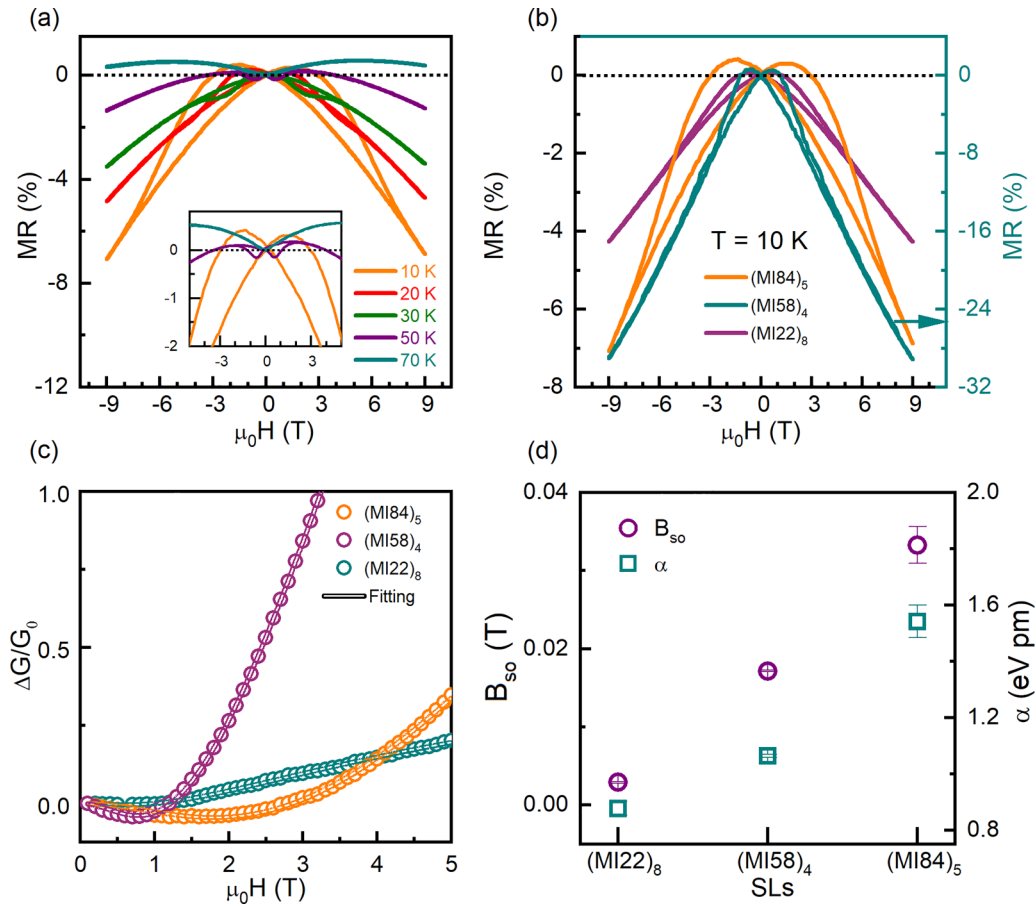


FIG. 1. (a) Magnetoresistance $MR(H)\% = \left[\frac{R(H)}{R(0)} - 1 \right] \times 100\%$ measured at various temperatures for $(MI84)_5$. For $H \parallel a$, MR was measured with the current applied along the in-plane ($H \perp a$) direction. (b) Comparison of MR at 10 K for $(MI_{xy})_z$ superlattices. Dashed lines in (a) and (b) denote $MR\% = 0$. (c) Quantum-corrected magnetoconductance ($\Delta G/G_0$) [$\Delta G(H) = G(H) - G(0)$] at $T = 10$ K with the fit to the Hikami-Larkin-Nagaoka (HLN) equation. Open symbols show experimental data, whereas solid lines represent the fit to HLN theory. (d) Variation in effective fields of spin-orbit coupling (SOC; B_{so}) scattering terms, and the Rashba SOC coefficient (α).

electron correlation U , resulting in increased resistivity and a canted AFM phase. Insulating CaMnO_3 too is a canted AFM in the same dimensions. In addition, both layers have a similar sense of structural distortion of (a^- , a^- , c^+) type in low dimensions. This combination of similarity of magnetic phase and structural distortion is a unique attribute and can be argued to be a decisive factor for a strong inter-layer coupling [16]. In these canted AFM heterostructures, Rashba SOC reconstructs the Berry curvature and enhances the intrinsic anomalous Hall conductivity by two orders of magnitude. The heterostructure with the pronounced strength of Rashba SOC shows the modulation in MA via the rotation of the magnetization easy axis. This modulation is remarkably controlled in a single architecture or superlattice and can be tuned over a broad range of temperatures and magnetic fields.

X-ray absorption spectroscopy (XAS) reveals that $[(\text{CaMnO}_3)_x/(\text{CaIrO}_3)_y]_z$ heterostructures [labeled $(MI_{xy})_z$, where M and I refer to CaMnO_3 and CaIrO_3 , respectively] exhibit thickness-dependent charge transfer across the interface. Results of this study reported in Ref. [16] confirm transfer of charge from Ir at the interface with Mn. These data further suggest that the charge transfer depends on the number of both CaIrO_3 and CaMnO_3 layers (and available carriers).

In this context, three superlattices— $(MI84)_5$, $(MI58)_4$, and $(MI22)_8$ —with the successive decrease in the charge transfer were chosen to understand the correlation of Rashba SOC in manipulating MA. Details of XAS and magnetization measurements are given in Ref. [16].

Figure 1(a) shows the magnetoresistance (MR) measured at various temperatures for $(MI84)_5$. At 50 K, a cusplike feature in the low-field region appears with definite butterfly hysteresis that broadens with decreasing temperature. Notably, <30 K, the hysteresis becomes nonmonotonic in the low-magnetic-field region, and at 20 K, the polarity of the peak resistivity in butterfly hysteresis reverses [inset, Fig. 1(a)]. This tentatively suggests a shift in the magnetization easy axis from the out-of-plane [100] to the in-plane [010] direction. A comparison in Fig. 1(b) reveals that, at 10 K, all three superlattices exhibit this cusplike feature. The temperature dependence of $MR(H)$ (Supplemental Material Fig. S1 [17]) suggests that, with decreasing charge transfer on moving from $(MI84)_5$ to $(MI22)_8$, the hysteresis appears at lower temperatures with no sign of peak polarity reversal.

For 2D systems, SOC is associated with weak antilocalization (WAL) [18,19], wherein the destructive interference of the backscattered electrons results in the cusplike feature

at the small magnetic field with positive MR. In contrast, negative MR in the high-magnetic-field region originates from weak localization (WL) due to the constructive backscattering of electrons [20,21]. The crossover from positive to negative MR with an increasing magnetic field suggests the simultaneous presence of SOC and WL in these heterostructures [22]. In such systems, Rashba SOC can be calculated according to the quantum correction theory of magnetoconductance associated with WAL [23]. To deduce charge-transfer-induced interfacial Rashba SOC in $\text{CaMnO}_3/\text{CaIrO}_3$ heterostructures, we plotted the normalized magnetoconductance $\frac{\Delta G(H)}{G_0}$ [Fig. 1(c)]. The coexistence of WAL and WL results in the minima in the magnetoconductance. The magnetic field associated with this minimum (B_{\min}) is roughly proportional to the strength of SOC [24]. As expected, with the increase in the charge transfer from $(MI22)_8$, $(MI58)_4$ to $(MI84)_5$, the cusp feature becomes more prominent, and the associated B_{\min} also increases, suggesting an increase in the Rashba SOC. A similar enhancement of the cusp feature has been observed in $\text{LaAlO}_3/\text{SrTiO}_3$ heterostructures under the application of a large electric field of 100 V [25,26].

Quantum-corrected magnetoconductance of a 2D system with SOC and WL at low perpendicular fields can be expressed by the Hikami-Larkin-Nagaoka (HLN) equation [23] as

$$\begin{aligned} \frac{\Delta G(B)}{G_0} = & -\psi\left(\frac{1}{2} + \frac{B_e}{B}\right) + \frac{3}{2}\psi\left(\frac{1}{2} + \frac{B_i + B_{so}}{B}\right) \\ & - \frac{1}{2}\psi\left(\frac{1}{2} + \frac{B_i}{B}\right) - \ln\left(\frac{B_i + B_{so}}{B_e}\right) \\ & - \frac{1}{2}\ln\left(\frac{B_i + B_{so}}{B_i}\right). \end{aligned}$$

Here, ψ is the digamma function, and G_0 is the universal conductance constant; 1.2×10^{-5} S. Also, B_e , B_i , and B_{so} are effective fields of elastic, inelastic, and SOC-induced scattering terms, respectively. The HLN fit of magnetoconductance in Fig. 1(c) depicts good agreement of the data with the theoretical model. We determined the Rashba SOC coefficient using the relation $\alpha = \frac{(e\hbar^2 B_{so})^{1/2}}{m^*}$, where $m^* = 3m_e$ is the effective mass of electron [27,28]. For the Ir-based oxide systems, m^* of the electron depends on film thickness due to the quantum confinement [29]. However, for IrO_2 , the change in m^* is found to be only 10–20% for the increase of film thickness from 3 to 9 monolayers. Similarly, for several other oxide and nonoxide systems too, m^* is found to be weakly dependent on the film thickness [30–36]. Hence, in this paper, we have considered m^* to be constant for all three superlattices. Thus, extracted parameters of B_{so} and α , as presented in Fig. 1(d), demonstrate the enhancement in Rashba SOC with the increase in the charge transfer fraction across the interface in $\text{CaMnO}_3/\text{CaIrO}_3$ heterostructures.

Figures 2(a)–2(b) show the Hall resistivity (ρ_{xy}) of $(MI84)_5$ and $(MI58)_4$ superlattices at various temperatures. Below 70 K, both heterostructures exhibit AHE with well-saturated hysteresis. Recent reports suggest that $3d-5d$ -based heterostructures with noncollinear AFM structure can exhibit AHE [37,38]. In materials having broken time-reversal symmetry in the presence of strong SOC, the intrinsic or extrinsic

origin of AHE can be deduced from the relationship between anomalous Hall resistivity (ρ_{xy}^{AHE}) and longitudinal resistivity (ρ_{xx}) [10,39]. A scattering rate-independent ρ_{xy}^{AHE} of intrinsic origin varies quadratically with respect to ρ_{xx} , whereas extrinsic AHE arising from the skew scattering varies linearly with ρ_{xx} [40–42]. The intrinsic AHE is associated with the topology of the electronic band structure via the Berry phase [39,43].

To deduce the origin of AHE in $\text{CaMnO}_3/\text{CaIrO}_3$ heterostructures, $\rho_{xy}^{\text{AHE}}(T)$ was plotted as a function of $\rho_{xx}^2(T)$ ($\mu_0 H = 0$) [Fig. 2(c)]. The value of $\rho_{xy}^{\text{AHE}}(T)$ was taken for $\mu_0 H = 9$ T, where both magnetization and ρ_{xy} are saturated. For $(MI84)_5$, a quadratic dependence between $\rho_{xy}^{\text{AHE}}(T)$ and ρ_{xx} indicates the scattering-independent intrinsic origin of AHE invoking the Berry phase, whereas for $(MI58)_4$, $\rho_{xy}^{\text{AHE}}(T)$ deviates from the quadratic dependence. Speculating the origin in skew scattering for $(MI58)_4$, ρ_{xy}^{AHE} was fitted linearly as a function of ρ_{xx} , but no satisfactory fit was obtained. However, $\sigma_{xx} \sim 150 - 180 \Omega^{-1} \text{cm}^{-1}$, as obtained from scaling behavior, puts $(MI58)_4$ into the moderately dirty metal limit. Based on the theoretical approach utilizing Berry curvature for SOC material in a moderately dirty metal region, the intrinsic scattering from the Berry phase yields ρ_{xy}^{AHE} independent of ρ_{xx} , a scenario that is not followed in the case of $(MI58)_4$ [9,44,45]. However, the $(MI58)_4$ superlattice does not show the expected scaling between $\rho_{xy}^{\text{AHE}}(T)$ and ρ_{xx} ; other $3d-5d$ heterostructures near the moderately dirty metal limit have been reported to show characteristic dissipation-less intrinsic AHE [9,45].

To get further insight into the origin of AHE, angular dependence of the Hall effect was measured [Fig. 2(d)]. The magnitude of AHE decreases as the magnetic field direction rotates in the yz plane with an angle θ away from the normal axis, indicating the intrinsic nature of AHE arising from the Berry phase in both $(MI84)_5$ and $(MI58)_4$ superlattices [46]. Similar behavior manifests in systems like Co single crystals, too [47]. At higher temperatures, the angle dependence of AHE decreases, suggesting the strength of Berry curvature reduces in accordance with the temperature dependence of AHE (Supplemental Material Fig. S2 [17]).

To understand the effect of Rashba SOC strength on AHE, we compare ρ_{xy}^{AHE} at 30 K for $(MI22)_8$, $(MI58)_4$, and $(MI84)_5$ (Fig. 3). AHE for $(MI22)_8$ is positive, with $\rho_{xy}^{\text{AHE}} > 0$ for $M > 0$. With an increase in Rashba SOC, the sign of AHE reverses, and a negative sense of AHE with $\rho_{xy}^{\text{AHE}} < 0$ for $M > 0$ is observed with increasing hysteresis coercivity. The magnitude of AHE also enhances systematically with increasing Rashba SOC. An overall two orders of magnitude increase from $(MI22)_8$ to $(MI84)_5$. Results of AHE show that interfacial Rashba SOC can greatly influence the electronic band properties of these heterostructures.

The *ab initio* calculations and XAS measurements reported in the literature suggest that, for $\text{CaMnO}_3/\text{CaIrO}_3$ interfaces, Mn-O-Mn interactions along the xy plane are ferromagnetic (FM) double exchange interaction, whereas Ir-O-Mn interactions are antiparallel superexchanges along the z direction [11]. Charge transfer across these interfaces can induce spin

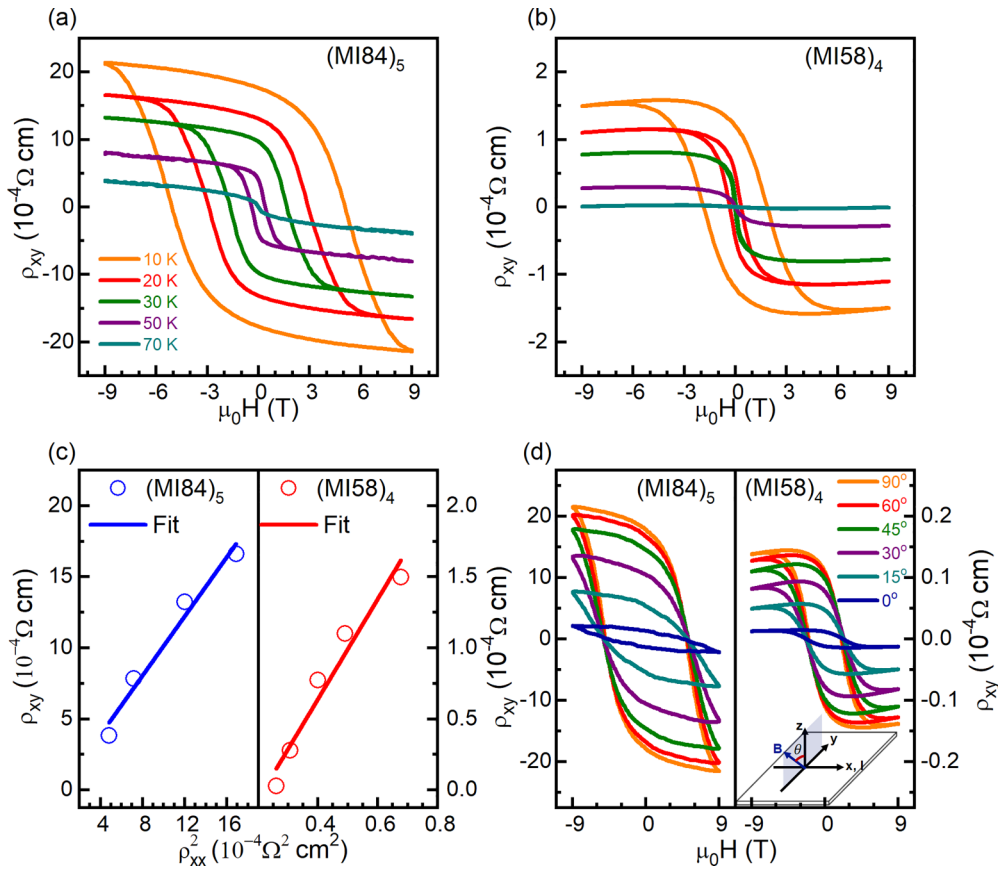


FIG. 2. Transverse Hall resistivity (ρ_{xy}) as a function of the perpendicular magnetic field measured at temperatures in the 10–70 K range for (a) $(MI84)_5$ and (b) $(MI58)_4$ superlattices. (c) Plots of ρ_{xy} vs ρ_{xx}^2 . Symbols represent the value of $\rho_{xx}(T)$ at $\mu_0 H = 0$ and $\rho_{xy}^{AHE}(T)$ for $\mu_0 H = 9$ T, where Hall resistivity is saturated. A solid line represents a straight line fit to the experimental data. (d) Angular dependence of anomalous Hall effect at $T = 10$ K. Inset depicts the rotation geometry of the magnetic field with the current applied perpendicular to the magnetic field.

polarization [$P_s = \frac{\text{DOS}_\uparrow(E_F) - \text{DOS}_\downarrow(E_F)}{\text{DOS}_\uparrow(E_F) + \text{DOS}_\downarrow(E_F)}$] due to larger DOS(E_F) resulting from the different effective masses in t_{2g} and e_g bands. This spin polarization and hence the AHE can be tuned via the fraction of charge transfer (x) across the interface. For low x , $P_s > 0$ results in the positive sense of AHE, while for higher x , $P_s < 0$ gives a negative sense of AHE.

The sign reversal of AHE can also be understood in terms of the relationship between the intrinsic AHE and the integration of Berry curvature Ω of all the occupied Bloch bands. In 2D FM materials, the motion of the electrons can be affected by the nonzero Berry curvature in momentum space, giving rise to intrinsic AHE. In that case, the Hall conductivity (σ_{xy}) can be calculated by integrating the Berry curvature Ω in the

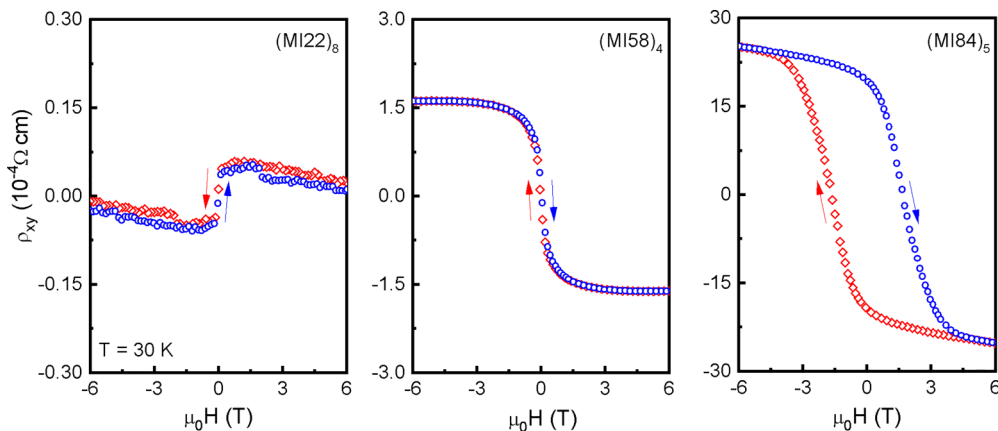


FIG. 3. Transverse Hall resistivity for $(MI22)_8$, $(MI58)_4$, and $(MI84)_5$ measured at $T = 30$ K.

first Brillouin zone as [39,48]

$$\sigma_{xy} = -\frac{e^2}{2\pi h} \int_{\text{BZ}} \Omega(\vec{k}) d^2\vec{k}.$$

Here, e is the elementary charge, h is the Planck constant, and \vec{k} is the momentum wave vector. Under the applied perpendicular magnetic field, the spontaneously ordered magnetic moments deviate the motion of electrons toward the high (low) potential side, and the intrinsic AHE with a positive (negative) sign emerges for $\int \Omega < 0$ ($\int \Omega > 0$). Thus, the sign reversal of AHE in $\text{CaMnO}_3/\text{CaIrO}_3$ interfaces suggests that Rashba SOC significantly influences the electronic band structure via the reconstruction of Berry curvature and the Berry phase.

Magnetization results on these heterostructures show the highest saturation moment for a thinner superlattice ($MI22$), which decreases with the increase in the thickness [16]. In contrast to magnetization, the stronger AHE is observed for the ($MI84$)₅ superlattice having the lowest magnetization. The fraction of the charge transfer influences the magnetic superexchange interaction in addition to the spin polarization. The Hamiltonian that depicts the magnetic moment alignment is given as [49]

$$\tilde{H} = -t \cos\left(\frac{\beta}{2}\right) \sum_{(ij)} (a_{i\uparrow}^\dagger a_{j\uparrow} + \text{H.c.}) \sum_{(ij)} J_{\text{ex}} (\hat{m}_i \cdot \hat{m}_j),$$

which simplifies into an energy equation $E = -4x|t|\cos(\frac{\beta}{2}) + J_{\text{ex}}\cos(\beta)$, where a^\dagger/a are the creation/annihilation operators, t is the hopping integral, β is the angle deviating from FM alignment, J_{ex} is the superexchange coupling, and x is the charge transfer fraction. Hence, the amount of the charge fraction x transferred across the interface decides the alignment of Mn magnetic moment in CaMnO_3 layers. For adequately high x , Mn and Ir moments are AFM coupled, while Mn is FM coupled [9,49]. However, low x results in the canted AFM ordering of Mn moments along the xy plane. Thus, ($MI84$)₅ has a higher Mn^{3+} and Mn^{4+} ratio with larger FM exchange of Mn moments, whereas in the bulk part of CaMnO_3 where charge transfer decays exponentially, AFM interactions are dominant. These results indicate that most of the AHE resides at the interface and within the CaMnO_3 layer.

The observed enhancement in AHE can also be correlated to the SOC strength. According to the first-order approximation, AHE is proportional to SOC [39], and therefore, the successive increase in the magnitude of AHE from ($MI22$)₈ to ($MI84$)₅ also augments the role of Rashba SOC in altering interfacial magnetism and electronic band structure in $\text{CaMnO}_3/\text{CaIrO}_3$ heterostructures. Similar results on the role of interface-induced Rashba SOC in modifying AHE have been reported for $p-i-n$ junctions, magnetic topological insulator heterostructures, etc. [13,50].

To probe the MA of $\text{CaMnO}_3/\text{CaIrO}_3$ heterostructures, anisotropic MR (AMR) was measured in a detailed temperature and magnetic field range. The applied magnetic field was rotated in the yz plane with respect to the superlattice, and AMR was calculated as

$$\text{AMR}(\%) = \frac{\rho[B(\theta)] - \rho[B(\theta = 90^\circ)]}{\rho[B(\theta = 90^\circ)]} \times 100\%,$$

where θ denotes the angle between the magnetic field and axis normal to the heterostructure. AMR measurements were carried out in the zero-field cooling protocol. Figure 4(a) presents thus measured AMR for ($MI84$)₅ at 25 K with varying magnetic field strengths. AMR exhibits twofold sinusoidal oscillations, while clockwise and counterclockwise rotation of the sample exhibits hysteresis in AMR oscillations (Supplemental Material Fig. S8 [17]).

The most remarkable feature of this AMR is the $\pi/2$ phase shift in the peak position accompanied by the sign reversal. For a low magnetic field, the minimum around $\theta = 180^\circ$ suggests that the easy axis is close to the out-of-plane direction [Fig. 4(a)]. Here, AMR is mostly positive. In the intermediate magnetic field range, the minima gradually shift toward lower θ with the positive-to-negative crossover in the AMR sign. For the higher field >7 T, a maximum phase shift of $\pi/2$ with the minima around $\theta = 90^\circ$ reveals that the easy axis is close to the in-plane direction. For ($MI84$)₅, this modulation in the MA is also observed as a function of temperature. The comparison of AMR polar plots in Fig. 4(b) for $T = 2$ and 40 K depicts a clear phase shift of $\pi/2$. Detailed comparison of AMR data is given in Supplemental Material Fig. S4 [17]. For ($MI84$)₅, this modulation of MA can be tuned systematically over a broad temperature and magnetic field ranges [Fig. 4(c)]. The scattered data point represents the dominant AMR% (i.e., dominance of AMR oscillation in the positive or negative region) in varying temperature and magnetic field ranges (red symbols for positive AMR and blue for negative AMR). The inset of Fig. 4(c) suggests that, for 2 K, AMR is negative throughout the range of magnetic fields. Circular symbols show the variation in AMR ratio with temperature for $\mu_0H = 9$ T. A transition in the sign reversal starts at 14 K. Magnetic field dependence for 20 and 30 K presented by square and diamond symbols, respectively, shows shifting of transition toward the lower magnetic field with increase in the temperature. A systematic shift in the phase reversal is seen from the data in Supplemental Material Fig. S4 [17]. For 50 K, a complete crossover of the easy axis close to the in-plane direction with a positive sign dominates for the entire magnetic field range [inset of Fig. 4(c)]. A close inspection of AMR oscillations in the range of 8–20 K reveals the modulation of MA via the slow and gradual rotation of the magnetization easy axis which starts to appear with the difference in the scattering intensities associated with the [100] and $[\bar{1}00]$ directions (Supplemental Material Fig. S5 [17]).

In Fig. 5(a), we compare AMR measured at various temperatures for $\mu_0H = 7$ T for all three superlattices. With the decrease in the strength of Rashba SOC from ($MI84$)₅ to ($MI58$)₄, the transition accommodating phase shift moves toward higher temperature, whereas no such magnetic-field-induced transition is observed throughout the temperature range of measurements for ($MI58$)₄ (Supplemental Material Fig. S6 [17]). For the weakest strength of Rashba SOC as in ($MI22$)₈, this transition vanishes completely (Supplemental Material Fig. S7 [17]). Further, in Supplemental Material Fig. S8 [17], we show the modulation of anisotropy in the superlattices with variation in the CaIrO_3 thickness. For the CaIrO_3 3 unit cell thickness in ($MI33$), we do not see any signature of the change in MA both as a function of magnetic field and temperature. For ($MI44$), a clear rotation of the

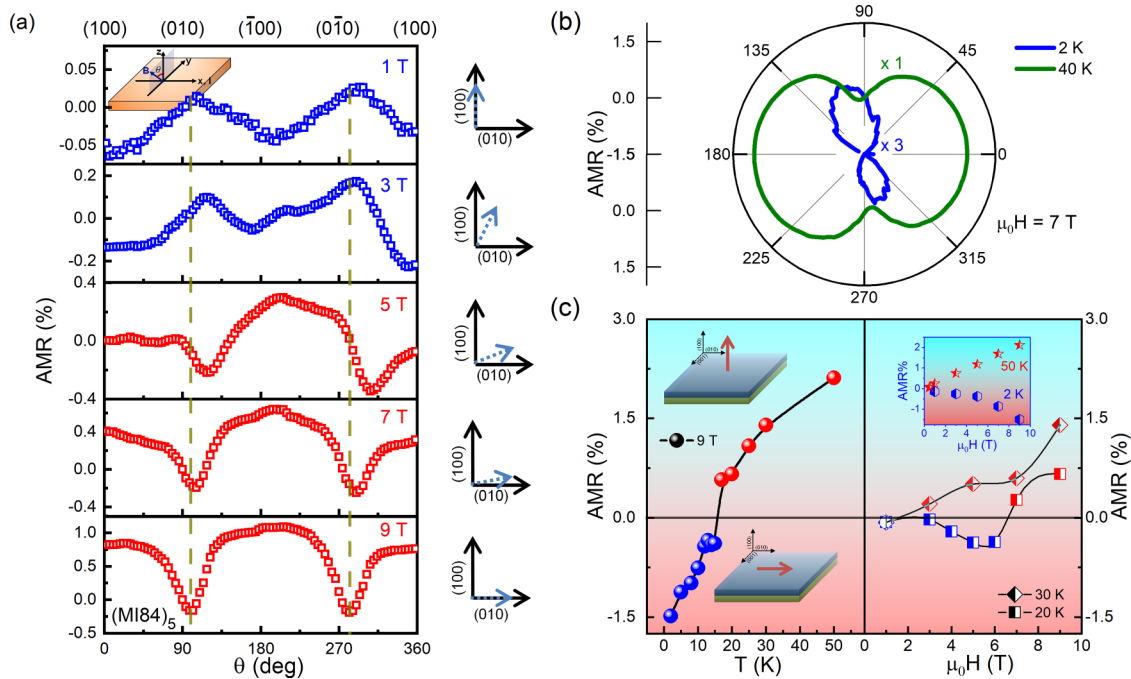


FIG. 4. (a) θ -anisotropic magnetoresistance (AMR) of $(MI84)_5$ at 25 K with increasing magnetic field strength. The schematic in the inset shows the applied magnetic field was rotated in the yz plane with respect to the superlattice and the current was passed along the pseudocubic [001] direction. A dashed line guides the modulation of the anisotropy with a magnetic field evident from the sign and phase change of AMR. (b) Polar plots comparing θ -AMR for $T = 2$ and 40 K ($\mu_0H = 7$ T) show a phase shift of $\pi/2$. (c) The scattered data point represents the dominance of AMR oscillation in the positive (red symbols) or negative region (blue symbols). AMR data for 2 and 50 K in the inset suggest an absence of magnetic-field-mediated rotation of the easy axis. Temperature dependence of AMR for $\mu_0H = 9$ T presented by circles.

magnetization easy axis is observed which supports the observation of modulation of anisotropy in $(MI84)$. Further, we also present the results of the $(MI82)$ superlattice which is a low CaIrO_3 thickness prototype of the $(MI84)$ superlattice; no modulation with MA is observed. The shift in the transition temperature with the strength of Rashba SOC in different

superlattices is demonstrated in the histogram in Fig. 5(b). To surmise, these data highlight the role of Rashba SOC in tailoring MA of the oxide heterostructures.

Recent efforts to modulate the magnetization easy axis have been achieved by tuning SOC, epitaxial strain, oxygen octahedra rotation, switching of noncollinear magnetic

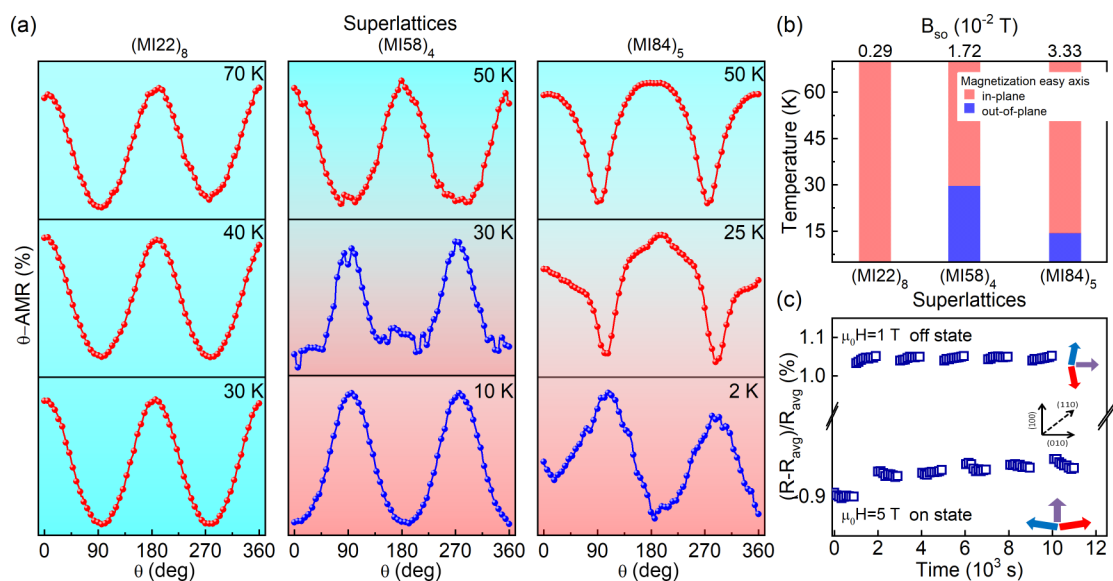


FIG. 5. (a) and (b) Temperature dependence of θ -anisotropic magnetoresistance (AMR) at $\mu_0H = 7$ T for $(MI84)_5$, $(MI58)_4$, and $(MI22)_8$ showing shift in the transition temperature with the strength of Rashba spin-orbit coupling (SOC). (c) Retention property of the switching between on and off states obtained by rotating the magnetization easy axis by magnetic field ($T = 30$ K, $\theta = 110^\circ$).

structure between AFM and FM states, and the spin-flop transition [51–55]. For example, rotation of the magnetization easy axis in $\text{La}_{2/3}\text{Sr}_{1/3}\text{MnO}_3/\text{SrIrO}_3$ heterostructures has been attributed to strong SOC mediated through the emergence of a spin-orbit state in SrIrO_3 [51]. Previous efforts to modulate MA were mainly focused on the FM materials or on the heterostructures interfacing FMs with the SOC materials. Further, the change in the magnetization easy axis has been obtained as a function of architecture of the heterostructure—a demonstration that requires several heterostructures. This presents a hindrance in realizing the spintronics-based devices utilizing MA as a key property. In this paper, we highlight the role of Rashba SOC in manifesting the modulation of MA in a single architecture of the canted AFM heterostructures which provides excellent groundwork for the development of desirable switching memory devices for AFM spintronics application. In the recent times, AFM materials have been proven to drive the technological change for their potential utility in the emerging field of AFM spintronics. On the other hand, Rashba physics-based phenomena have been the cynosure of the upcoming field of spin-orbitronics. Both areas present an opportunity for the development of energy-efficient devices with faster operationality. In this paper, we combine these two important features in one system, enhancing the fundamental understanding for the development of multifunctional devices having unified control of Rashba SOC.

In Fig. 5(c), retention properties of the anisotropic resistive states show nonvolatile switching, where the on and off states were obtained by reorientation of the easy axis from the out-of-plane to the in-plane direction by switching the magnetic field between 1 and 5 T, respectively (Supplemental Material Figs. S9 and S10 [17]). Extrinsic contributions such

as the presence of an EB field can also alter the MA of the materials [56]. The role of the EB field of 35 Oe in $(\text{MI}84)_5$ is also evaluated in detail in Supplemental Material Figs. S11 and S12 [17]. For two reasons, the contribution of EB can be expected to be negligible: (i) For the maximum EB at 10 K, $(\text{MI}84)_5$ exhibits minimum modulation in anisotropy; and (ii) absence of EB in the $(\text{MI}58)_4$ heterostructure shows the change in MA.

In conclusion, we show the effective tuning of transport phenomena at $3d-5d$ interfaces by Rashba SOC. Berry-phase-driven spin texture and MA can be engineered by the pronounced SOC in the absence of an electric field. Switching between these anisotropy-governed resistance states offers a perspective to design nonvolatile multifunctional memory devices. In this paper, we also provide the ground to formulate desirable control of Rashba SOC without applied bias voltage for operational spin-orbitronics application.

D.S.R. thanks Science and Engineering Research Board Technology, New Delhi, for financial support under Project No. CRG/2020/002338. M.V. acknowledges the Department of Science and Technology (DST), New Delhi, India, for the INSPIRE faculty award (No. DST/INSPIRE/04/2017/003059). J.S. acknowledges the DST-INSPIRE for the Fellowship (No. DST/INSPIRE/03/2018/000699). The authors thank Dr. Ravi Shankar Singh (IISER Bhopal), Dr. Gulloo Lal Prajapati (Helmholtz-Zentrum Dresden-Rossendorf, Germany), Dr. T. Suraj (NUS, Singapore), and Dr. Ganesh Ji Omar (NUS, Singapore) for fruitful discussions.

The authors declare no competing interests.

-
- [1] P. W. Anderson, *Science* **177**, 393 (1972).
- [2] L. D. Landau, *Phys. Z. Sowjetunion* **11**, 542 (1937).
- [3] A. Manchon, H. C. Koo, J. Nitta, S. M. Frolov, and R. A. Duine, *Nat. Mater.* **14**, 871 (2015).
- [4] D. C. Vaz, P. Noël, A. Johansson, B. Göbel, F. Y. Bruno, G. Singh, S. Mckeown-Walker, F. Trier, L. M. Vicente-Arche, A. Sander *et al.*, *Nat. Mater.* **18**, 1187 (2019).
- [5] F. Trier, P. Noël, J. V. Kim, J. P. Attané, L. Vila, and M. Bibes, *Nat. Rev. Mater.* **7**, 258 (2021).
- [6] F. T. Vas'ko, *P. Zh. Eksp. Teor. Fiz.* **30**, 574 (1979) [*JETP Lett.* **30**, 541 (1979)].
- [7] Y. A. Bychkov and E. I. Rashba, *P. Zh. Eksp. Teor. Fiz.* **39**, 66 (1984).
- [8] D. Xiao, M.-C. Chang, and Q. Niu, *Rev. Mod. Phys.* **82**, 1959 (2010).
- [9] J. Nichols, X. Gao, S. Lee, T. L. Meyer, J. W. Freeland, V. Lauter, D. Yi, J. Liu, D. Haskel, J. R. Petrie *et al.*, *Nat. Commun.* **7**, 12721 (2016).
- [10] M. W. Yoo, J. Tornos, A. Sander, L. F. Lin, N. Mohanta, A. Peralta, D. Sanchez-Manzano, F. Gallego, D. Haskel, J. W. Freeland *et al.*, *Nat. Commun.* **12**, 3283 (2021).
- [11] Z. S. Lim, C. Li, Z. Huang, X. Chi, J. Zhou, S. Zeng, G. J. Omar, Y. P. Feng, A. Rusydi, S. J. Pennycook *et al.*, *Small* **16**, 2004683 (2020).
- [12] E. Skoropata, J. Nichols, J. M. Ok, R. V. Chopdekar, E. S. Choi, A. Rastogi, C. Sohn, X. Gao, S. Yoon, T. Farmer *et al.*, *Sci. Adv.* **6**, eaaz3902 (2020).
- [13] F. Wang, X. Wang, Y. F. Zhao, D. Xiao, L. J. Zhou, W. Liu, Z. Zhang, W. Zhao, M. H. Chan, N. Samarth *et al.*, *Nat. Commun.* **12**, 79 (2021).
- [14] D. Stornaiuolo, C. Cantoni, G. M. D. Luca, R. D. Capua, G. Ghiringhelli, B. Jouault, D. Marrè, D. Massarotti, F. M. Granozio, I. Pallecchi *et al.*, *Nat. Mater.* **15**, 278 (2016).
- [15] G. Herranz, G. Singh, N. Bergeal, A. Jouan, J. Lesueur, J. Gázquez, M. Varela, M. Scigaj, N. Dix, F. Sánchez *et al.*, *Nat. Commun.* **6**, 6028 (2015).
- [16] M. Vagadia, S. Sardar, T. Tank, S. Das, B. Gunn, P. Pandey, R. Hübner, F. Rodolakis, G. Fabbris, Y. Choi *et al.*, *Phys. Rev. B* **105**, L020402 (2022).
- [17] See Supplemental Material at <http://link.aps.org/supplemental/10.1103/PhysRevB.107.064420> for additional anisotropic transport and magneto-transport data.
- [18] G. Bergmann, *Phys. Rep.* **107**, 1 (1984).
- [19] P. D. Dresselhaus, C. M. A. Papavassiliou, R. G. Wheeler, and R. N. Sacks, *Phys. Rev. Lett.* **68**, 106 (1992).
- [20] M. Li, R. Yang, X. Wei, H. Yin, S. Wang, and K. Jin, *ACS Appl. Mater. Interfaces* **13**, 21964 (2021).
- [21] Y. Gan, Y. Zhang, D. V. Christensen, N. Pryds, and Y. Chen, *Phys. Rev. B* **100**, 125134 (2019).

- [22] T. S. Suraj, G. J. Omar, H. Jani, M. M. Juvaid, S. Hooda, A. Chaudhuri, A. Rusydi, K. Sethupathi, T. Venkatesan, A. Ariando *et al.*, *Phys. Rev. B* **102**, 125145 (2020).
- [23] S. Hikami, A. I. Larkin, and Y. Nagaoka, *Prog. Theor. Phys.* **63**, 707 (1980).
- [24] S. Faniel, T. Matsuura, S. Mineshige, Y. Sekine, and T. Koga, *Phys. Rev. B* **83**, 115309 (2011).
- [25] A. D. Caviglia, M. Gabay, S. Gariglio, N. Reyren, C. Cancellieri, and J. M. Triscone, and J.M, *Phys. Rev. Lett.* **104**, 126803 (2010).
- [26] D. Stornaiuolo, S. Gariglio, A. Fete, M. Gabay, D. Li, D. Massarotti, and J. M. Triscone, *Phys. Rev. B* **90**, 235426 (2014).
- [27] D. N. Basov, R. D. Averitt, D. Van Der Marel, M. Dressel, and K. Haule, *Rev. Mod. Phys.* **83**, 471 (2011).
- [28] C. Schierholz, T. Matsuyama, U. Merkt, and G. Meier, *Phys. Rev. B* **70**, 233311 (2004).
- [29] J. K. Kawasaki, C. H. Kim, J. N. Nelson, S. Crisp, C. J. Zollner, E. Biegenwald, J. T. Heron, C. J. Fennie, D. G. Schlom, and K. M. Shen, *Phys. Rev. Lett.* **121**, 176802 (2018).
- [30] A. T. Hatke, M. A. Zudov, J. D. Watson, M. J. Manfra, L. N. Pfeiffer, and K. W. West, *Phys. Rev. B* **87**, 161307(R) (2013).
- [31] L. Smrčka, P. Vašek, J. Koláček, T. Jungwirth, and M. Cukr, *Phys. Rev. B* **51**, 18011 (1995).
- [32] N. Olszowska, J. Lis, P. Ciochon, Ł. Walczak, E. G. Michel, and J. J. Kolodziej, *Phys. Rev. B* **94**, 115305 (2016).
- [33] T. C. Chiang, *Surf. Sci. Rep.* **39**, 181 (2000).
- [34] M. A. Mueller, T. Miller, and T. C. Chiang, *Phys. Rev. B* **41**, 5214 (1990).
- [35] W. Meevasana, P. D. C. King, R. H. He, S. K. Mo, M. Hashimoto, A. Tamai, P. Songsiriritthigul, F. Baumberger, and Z. X. Shen, *Nat. Mater.* **10**, 114 (2011).
- [36] A. F. Santander-Syro, O. Copie, T. Kondo, F. Fortuna, S. Pailhes, R. Weht, X. G. Qiu, F. Bertran, A. Nicolaou, A. Taleb-Ibrahimi *et al.*, *Nature (London)* **469**, 189 (2011).
- [37] S. Nakatsuji, N. Kiyohara, and T. Higo, *Nature (London)* **527**, 212 (2015).
- [38] N. J. Ghimire, A. S. Botana, J. S. Jiang, J. Zhang, Y.-S. Chen, and J. F. Mitchell, *Nat. Commun.* **9**, 3280 (2018).
- [39] N. Nagaosa, J. Sinova, S. Onoda, A. H. MacDonald, and N. P. Ong, *Rev. Mod. Phys.* **82**, 1539 (2010).
- [40] L. Berger, *Phys. Rev. B* **2**, 4559 (1970).
- [41] J. Smit, *Physica* **21**, 877 (1955).
- [42] J. Smit, *Physica* **24**, 39 (1958).
- [43] F. D. M. Haldane, *Phys. Rev. Lett.* **93**, 206602 (2004).
- [44] S. Onoda, N. Sugimoto, and N. Nagaosa, *Phys. Rev. B* **77**, 165103 (2008).
- [45] W. L. Lee, S. Watauchi, V. L. Miller, R. J. Cava, and N. P. Ong, *Science* **303**, 1647 (2004).
- [46] D. Zhang, Y. Wang, N. Lu, X. Sui, Y. Xu, P. Yu, and Q.-K. Xue, *Phys. Rev. B* **100**, 060403(R) (2019).
- [47] E. Roman, Y. Mokrousov, and I. Souza, *Phys. Rev. Lett.* **103**, 097203 (2009).
- [48] H. Weng, R. Yu, X. Hu, X. Dai, and Z. Fang, *Adv. Phys.* **64**, 227 (2015).
- [49] S. Bhowal and S. Satpathy, *Phys. Rev. B* **99**, 245145 (2019).
- [50] A. C. Yang, S. S. Yan, K. Zhang, H. H. Li, J. Pei, L. M. He, Y. F. Tian, Y. F. Qin, S. S. Kang, and S. Q. Xiao, *RSC Adv.* **6**, 55930 (2016).
- [51] D. Yi, J. Liu, S.-L. Hsu, L. Zhang, Y. Choi, J.-W. Kim, Z. Chen, J. D. Clarkson, C. R. Serrao, E. Arenholz *et al.*, *Proc. Natl. Acad. Sci. USA* **113**, 6397 (2016).
- [52] D. Yi, C. L. Flint, P. P. Balakrishnan, K. Mahalingam, B. Urwin, A. Vailionis, A. T. N'Diaye, P. Shafer, E. Arenholz, Y. Choi *et al.*, *Phys. Rev. Lett.* **119**, 077201 (2017).
- [53] D. Tian, Z. Liu, S. Shen, Z. Li, Y. Zhou, H. Liu, H. Chen, and P. Yu, *Proc. Natl. Acad. Sci. USA* **118**, e2101946118 (2021).
- [54] J. D. Hoffman, S. M. Wu, B. J. Kirby, and A. Bhattacharya, *Phys. Rev. Appl.* **9**, 044041 (2018).
- [55] H. Wang, C. Lu, J. Chen, Y. Liu, S. L. Yuan, S.-W. Cheong, S. Dong, and J.-M. Liu, *Nat. Comm.* **10**, 2280 (2019).
- [56] J. Nogués and I. K. Schuller, *J. Magn. Magn. Mater.* **192**, 203 (1999).